Quantum versus classical chirps in a Rydberg atom

Tsafrir Armon and Lazar Friedland [*]

Racah Institute of Physics, Hebrew University of Jerusalem, Jerusalem 91904, Israel

The interplay between quantum-mechanical and classical evolutions in a chirped-driven Rydberg atom is discussed. It is shown that the system allows two continuing resonant excitation mechanisms, i.e., a successive two-level transitions (ladder climbing) and a continuing classicallike nonlinear phase locking (autoresonance). The persistent 1:1 and 2:1 resonances between the driving and the Keplerian frequencies are studied in detail and characterized in terms of two dimensionless parameters $P_{1,2}$ representing the driving strength and the nonlinearity in the problem, respectively. The quantum-mechanical rotating wave and the classical single-resonance approximations are used to describe the regimes of efficient classical or quantum-mechanical excitation in this two-parameter space.

I. INTRODUCTION

Rydberg atoms possess many unique properties. With their large principal quantum number, $n \gg 1$, they exhibit a long radiative lifetime (scaling as n^3), a large orbital radius and dipole moment (scaling as n^2), and more (see [1] and references therein). As a result, they show great promise in many applications including quantum nondemolition measurements of photons [2], digital communication [3], measurement of microwave fields [4,5], quantum information (see [6] for a comprehensive review), and more. The ability to manipulate and control Rydberg atoms is thus of great importance.

Of particular interest are circular Rydberg states (CRSs), i.e., Rydberg atoms in states with $l = n - 1$, where l is the orbital quantum number and m, the magnetic quantum number, can take any value $|m| \leqslant n - 1$. Such states have the longest radiative lifetime and magnetic moment [7], which makes them better suited for many applications. Various techniques for the creation of CRSs have been proposed and implemented over the years [7–10]. CRSs have been used in several innovative advances in cavity quantum electrodynamics [11,12] and are proposed for future applications like quantum simulators of many-body physics [13].

In recent years, chirped frequency drives were studied as a tool for control and manipulation of various oscillatory systems, including Rydberg atoms [14–18]. In many cases, the response of the system to the chirped drive could take a quantum-mechanical, classical, or mixed form. In the classical limit, a persistent nonlinear phase locking between the driver and the system, known as autoresonance (AR) [19], yields a continuing excitation. In contrast, in the quantum limit, the system undergoes successive Landau-Zener (LZ) transitions [20,21], i.e., the quantum energy ladder-climbing (LC). Both regimes of operation have been demonstrated and used in atoms and molecules [22–26], Josephson junctions [27], plasma waves [28,29], discrete nonlinear systems [30], and cold neutrons [31].

In this work, we study the effects of a linearly polarized, chirped frequency electric field on a Rydberg atom initialized in a CRS. Even though we usually associate large quantum numbers with the emergence of classical phenomena, we show that it is not a sufficient condition. Particularly, Rydberg atoms in a CRS, while having $n, l \gg 1$, can exhibit both classical and quantum-mechanical responses to the chirped drive.

We describe the characteristics of quantum-mechanical persistent resonance and compare it to the previously studied case of classical autoresonance [15,32]. With the use of a unified parametrization, the necessary conditions for each resonant regime are mapped, allowing one to easily determine what evolution should be expected for a given parameter choice and when each regime is accessible. The persistent 1:1 and 2:1 resonances between the driving and the Keplerian frequency of the atom are discussed in detail.

The scope of the paper is as follows: In Sec. II, we introduce the model and its parametrization. Section III characterizes the resonant structure of the problem and Sec. IV analyzes the quantum and classical resonant regimes and the associated parameter space for the 1:1 resonance. Section V builds on Sec. IV and analyzes the 2:1 resonance, while our conclusions are summarized in Sec. VI.

II. THE MODEL AND PARAMETERIZATION

We consider a Rydberg atom driven by an oscillating electric field of constant amplitude and a down chirped frequency ω_d such that $d\omega_d/dt = -\alpha$, with α being a constant chirp rate. The Hamiltonian of the problem $\hat{H} = \hat{H}_0 + \hat{U}$ includes the usual unperturbed part

$$\hat{H}_0 = \frac{\hat{\bar{p}}^2}{2m_e} - \frac{e^2}{\hat{r}}, \tag{1}$$

and the driving part $\hat{U} = \varepsilon \cos \phi_d \hat{z}$, where m_e and e are the electron's mass and charge, ε and $\phi_d = \int_0^t \omega_d(t')dt'$ are the driving amplitude and phase, respectively, and the driving field is in the z direction. The operator $\hat{z}$ is dimensionless,

*lazar@mail.huji.ac.il

with the normalization constant included in ε. The eigenfunctions $|n, l, m\rangle$ of $\hat{H}_0$ satisfy $\hat{H}_0|n, l, m\rangle = E_n|n, l, m\rangle$, where $E_n = -R_y n^{-2}$ and R_y is the Rydberg energy. Note that we neglected the corrections to the energy due to other quantum defects [33,34], as they are fairly constant and do not have notable consequences for this work. As an initial condition we consider a single $|n_0, n_0 - 1, m\rangle$ CRS.

The resonances in the problem are studied in detail in Sec. III, but their nature is important for the choice of a suitable parametrization. These resonances correspond to a q:1 ratio between ω_d and the Keplerian frequency (approximately given by $\frac{dE_n}{dn}/\hbar$), and they affect transitions between the states $|n, l, m\rangle \leftrightarrow |n + q, l + 1, m\rangle$, which are coupled due to the driving field via normalized coupling coefficients,

$$c_{n,l,m}^{\pm q} = \frac{\langle n, l, m|\hat{z}|n \pm q, l \pm 1, m\rangle}{C_0}, \qquad (2)$$

where $C_0 = |\langle n_0, n_0 - 1, m|\hat{z}|n_0 + q, n_0, m\rangle|$. Note that because of the z polarization of the driving field, m is conserved throughout the evolution while l is only coupled to $l \pm 1$. Due to the strong nonlinearity of the coupling coefficients and E_n with respect to n, many quantities in the problem may change by orders of magnitude when n varies. Therefore, every parametrization will always be, in some sense, local—helping one to study the vicinity of a specific value of n.

For the initial condition comprised of a single $|n_0, n_0 - 1, m\rangle$ CRS, one can identify three time scales in the initial setting of the problem, i.e., the nonlinearity time scale $T_{\rm nl} = q^2|\frac{d^2 E_{n_0}}{dn_0^2}|/\hbar\alpha$ approximating the time between the first two successive transitions, the frequency sweep time scale $T_s = \alpha^{-1/2}$ and the Rabi time scale $T_R = 2\hbar/C_0\varepsilon$. Using these three time scales we define the dimensionless time $\tau = t/T_s = t\sqrt{\alpha}$ and two dimensionless parameters

$$P_1 = \frac{T_s}{T_R} = \frac{C_0\varepsilon}{2\hbar\sqrt{\alpha}}, \qquad (3)$$

$$P_2 = \frac{T_{\rm nl}}{T_s} = \frac{6q^2 R_y}{\hbar\sqrt{\alpha}n_0^4}, \qquad (4)$$

characterizing the driving strength and the nonlinearity in the problem, respectively. The parameters $P_{1,2}$ fully define the evolution of the system. Indeed, upon expansion of the wave function in terms of the eigenfunctions $|\psi\rangle = \sum_{n,l,m} a_{n,l,m}|n, l, m\rangle$ one can write the dimensionless Schrödinger equation for the coefficients $a_{n,l,m}$,

$$i\frac{da_{n,l,m}}{d\tau} = \overline{E}_n a_{n,l,m} + 2P_1 \cos\phi_d \sum_{n'} \sum_{\Delta l=\pm 1} c_{n,l,m}^{n',l'} a_{n',l',m}, \quad (5)$$

where now $\overline{E}_n$ is the dimensionless energy $-P_2 n_0^4/6q^2 n^2$, $l' = l + \Delta l$, and the summation over n', Δl follows the restrictions on the quantum numbers, i.e., $n' \geqslant 1, 0 \leqslant l' < n', |m| \leqslant l'$.

The resonant dynamics emerging from Eq. (5) are the main focus of this work, and it is helpful to first examine the different types of evolutions one can expect when changing the parameters $P_{1,2}$. As a representative example, we choose the 1:1 resonance, with a single CRS initial condition: $n_0 = 40$, $l_0 = n_0 - 1 = 39$, $m = l_0 = 39$. Figure 1 shows the numerical solution of Eq. (5) for $P_1 = 1, P_2 = 30$. (For details on the numerical simulations see Appendix B.) At time $\tau = 0$ the
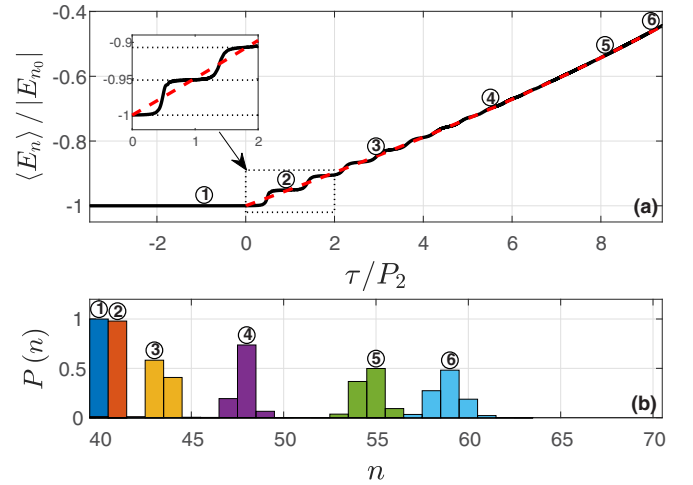

FIG. 1. Quantum-mechanical numerical simulation of the 1:1 resonance dynamics for an initial CRS with $n_0 = 40$, $m = 39$. The parameters are $P_1 = 1$, $P_2 = 30$. (a) Expectation value of the unperturbed energy as a function of time, normalized by the magnitude of the initial energy (solid black line). The dashed red line represents the resonance condition, (7). Inset: Zoom-in of the region in the dotted box. Dotted lines show the normalized energy of states n_0, $n_0 + 1$, and $n_0 + 2$. (b) Population of states with different n's, for six times during the evolution as defined in (a).

driving frequency passes the resonance with the Keplerian frequency $d\overline{E}_n/dn$ associated with n_0.

Figure 1(a) shows the average unperturbed energy $\langle\overline{E}_n\rangle = \sum_{n,l} \overline{E}_n|a_{n,l,m}|^2$ normalized with respect to the initial energy $|\overline{E}_{n0}|$, as a function of time and one can see a continuing increase in the energy of the system at later times. Furthermore, the initial growth of the energy proceeds in sharp "jumps" as highlighted in the inset. The dashed lines in the inset show the unperturbed energies $\overline{E}_{n_0}$, $\overline{E}_{n_0+1}$, $\overline{E}_{n_0+2}$ normalized by $|\overline{E}_{n_0}|$. The sharp transitions between these energy values indicate a full population transfer between neighboring n states. As a further illustration, Fig. 1(b) shows the distribution of the population between the different n values, $P_n = \sum_l |a_{n,l,m}|^2$, at six specific times, corresponding to markers 1, 2 ..., 6 in Fig. 1(a). Comparing the distributions at times 1 and 2 in the figure, one can observe a full population transfer between n_0 and $n_0 + 1$ states. This trend continues at time 3, which is in the middle of a two-level transition. However, later the energy growth smooths, and the distribution $P(n)$ broadens—revealing multilevel transitions in the system.

Next, we compare the results in Fig. 1 with those in Fig. 2, corresponding to the same initial conditions and parameters, but $P_2 = 30$ instead of 0.6. Figure 2(a) still exhibits an energy increase, but no sharp "jumps" associated with two-level transitions are observed. Additionally, the distributions $P(n)$ in Fig. 2(b) become wide shortly after the beginning of the process and much wider than in Fig. 2(b) at the final times. Such wide distributions are indicative of classicallike behavior. This is illustrated in Fig. 2(a), where the gray shaded area represent 100 classical trajectories with the corresponding initial conditions and uniformly distributed initial driving phases (the details of the classical simulation are given in Appendix B) and one observes that the quantum-mechanical
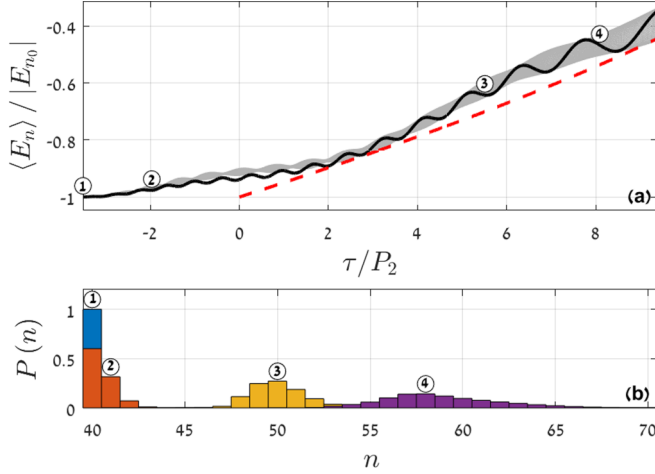
FIG. 2. The same as Fig. 1, but for $P_2 = 0.6$. The gray shaded area in (a) is comprised of 100 classical trajectories with corresponding classical initial conditions and uniformly distributed initial driving phases. The dashed red line in (a) represents the resonance condition, (7).

energy of the system with $P_2 = 30$ follows closely the classical evolution. It should be noted that the oscillations visible in the quantum-mechanical solution in this case have twice the driving frequency and, thus, represent a nonresonant effect.

In the following sections we show that indeed the dynamics in Fig. 1 represents a quantum-mechanical LC process, while that in Fig. 2 corresponds to the classical AR. We describe how Eq. (5) yields the aforementioned two types of evolutions and discuss the resonant excitation efficiency in the problem in our $P_{1,2}$ parameter space.

III. RESONANT STRUCTURE

We have illustrated above that the response of our system to the chirped drive is dominated by resonant interactions. These resonances can be studied conveniently via transformation to a rotating frame of reference and application of the rotating-wave approximation (RWA) to neglect all rapidly oscillating terms in Eq. (5). To this end, we define $b_{n,l,m} = a_{n,l,m}e^{il\phi_d}$, which transforms Eq. (5) into

$$i\frac{db_{n,l}}{d\tau} \approx -\Gamma_{n,l}b_{n,l} + P_1\big[c_{n,l}^{+q}b_{n+q,l+1} + c_{n,l}^{-q}b_{n-q,l-1}\big], \quad (6)$$

where index m was omitted for brevity and $\Gamma_{n,l} = \overline{E}_n + l\omega_d$. In this rotating frame of reference only the states with similar pseudoenergies $\Gamma_{n,l}$ are resonant, while all other states oscillate rapidly and can be neglected. The resonance condition between states n, l and states $n + q, l + 1$ is then given by equating $\Gamma_{n,l} = \Gamma_{n+q,l+1}$. In the limit of large n, one finds this condition to be

$$\omega_d \approx q\frac{d\overline{E}_n}{dn}, \quad (7)$$

which, as mentioned above, corresponds to a q:1 ratio between the driving frequency and the Keplerian frequency $d\overline{E}_n/dn$. Since $\omega_d = \omega_0 - \tau$ (here and below we use ω_d and ω_0 normalized by $1/T_s = \sqrt{\alpha}$), it is possible to solve for the value of n satisfying the resonance condition, (7), as a function of the

time and use it to define the resonant value for the energy. The dashed red lines in Figs. 1 and 2 show this resonant energy as a function of the time and we observe that the evolution of the energy of the system follows closely the resonant energy.

When neglecting rapidly oscillating terms in Eq. (6), one must verify that other pseudoenergy crossings (for different resonance ratios q) do not interfere with the desired resonant chain. To this end, we define the time τ_n^q when the resonance condition, (7), is met for the transition $n, l \leftrightarrow n + q, l + 1$. Note that since $d\overline{E}_n/dn$ is monotonic in n, the resonant transitions along a given resonant chain are ordered consecutively (i.e., $\tau_n^q < \tau_{n+q}^q$). Nevertheless, if τ_{n+q}^{q+1} is larger than τ_n^q but smaller than τ_{n+q}^q, the two resonant chains will mix. This leads to two conditions which must be met to avoid this mixing, i.e., $\tau_{n+q}^{q+1} > \tau_n^q$ and $\tau_{n+q}^q < \tau_{n+q}^{q+1}$. One can show that the first condition is always met, while the second is only true starting from some minimal n value. This minimal n can be found numerically, and above this n the resonant chains do not mix. For example, the minimal n is 6, 17, and 34 for $q = 1, 2$, and 3, respectively [35]. Within the RWA, when the resonant chains are separated, one can study them individually, and this is what we do next.

IV. 1:1 RESONANCE

Section II illustrated that parameter P_2 may change the nature of the evolution of the system, and that two efficient excitation regimes are possible. However, such efficient excitation is not guaranteed and depends on the choice of parameters $P_{1,2}$. To further understand this effect, we now discuss the excitation efficiency of the 1:1 resonance for a CRS initial condition with maximal m, i.e., $m = l_0 = n_0 - 1$. As a measure for the efficiency we examine the fraction of excited population with n exceeding a certain threshold value n_{th} at the final time of evolution. We proceed and show the numerical solution of Eq. (6) for the distribution of the excitation efficiency in $P_{1,2}$ parameter space in Fig. 3(a). The initial (final) driving frequency in these simulations is given by Eq. (7) for $n = 30$ ($n = 60$), while $n_{th} = 50$ and the initial condition is a single CRS with $n_0 = 40$ and $m = l_0 = 39$. The choice of n_0 puts the transition frequencies in the readily accessible microwave regime, while the choice of n_{th} is discussed in Sec. IV C.

As expected, the higher the driving amplitude (characterized by P_1), the higher the excitation efficiency, up to 100%. However, the gradual transition from no excitation to full excitation happens in the vicinity of two distinct lines in the parameter space, represented by the dashed diagonal line and the dashed-dotted vertical line. Clearly, this hints at two different resonant mechanisms in play and their study is our next goal.

A. Quantum-mechanical ladder-climbing

Motivated by the two-level transitions shown in Fig. 1, we analyze Eq. (6) again, but this time for two neighboring levels only,

$$i\frac{d}{d\tau}\begin{pmatrix} b_n \\ b_{n+1} \end{pmatrix} = \begin{pmatrix} \overline{E}_n - (n-1)\tau & P_1 c_n^{+1} \\ P_1 c_n^{+1} & \overline{E}_{n+1} - n\tau \end{pmatrix}\begin{pmatrix} b_n \\ b_{n+1} \end{pmatrix}, \quad (8)$$
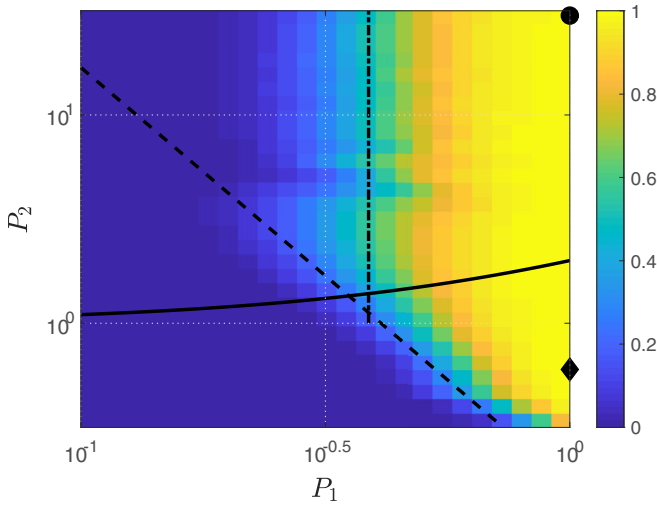
FIG. 3. Quantum-mechanical numerical simulations for the 1:1 resonance case. Equation (6) is solved for the fraction of population with $n > 50$ when starting from a CRS with $n_0 = 40$ and $m = 39$. The circle (diamond) show the parameters used in Fig. 1 (Fig. 2). The initial (final) driving frequency matches the resonant frequency at $n = 30$ ($n = 60$). The dashed line mark the classical threshold, (14). The solid line mark the quantum-classical separation line, (11). The dashed-dotted line marks the value of $P_{1,th}^{LC}$ as calculated using Eq. (9).

where index l was omitted because the difference $n - l$ is conserved at 1 along the 1:1 resonance chain starting from a CRS. The initial driving frequency was omitted from ω_d in (8) for brevity, as it could be canceled by shifting time. Equation (8) describes a two-level Landau-Zener transition [20,21]. If the transitions' times, as found from Eq. (7), are well separated, the system will undergo successive LZ transitions, commonly known as quantum energy LC. This explains the initial dynamics shown in Fig. 1(a). To see the relevance of the LC process to the parameter space of Fig. 3 one needs to examine the efficiency of the process. The efficiency of a single LZ transition, i.e., the fraction of the population transferring from level n to level $n + 1$, depends on P_1 only and is given by the LZ formula $1 - \exp\left[-2\pi\left(P_1 c_n^{+1}\right)^2\right]$. Indeed, one can see in Fig. 3 that for large values of P_2, the efficiency of the excitation is independent of P_2. Furthermore, one can find the efficiency of the full LC process, by multiplying the efficiencies of successive single transitions:

$$P = \prod_{n=n_0}^{n_{th}} 1 - \exp\left[-2\pi\left(P_1 c_n^{+1}\right)^2\right]. \tag{9}$$

By setting Eq. (9) equal to $1/2$ we can define the threshold value $P_{1,th}^{LC}$ for which half the population will reach the target state n_{th}. In principle, this value depends on n_{th}, but for the parameters of this problem within a few transitions c_n^{+1} scales as $n^2/n_0^{3/2}$, so the product, (9), converges rapidly and only weakly depends on n_{th}. One finds numerically that $P_{1,th}^{LC} \approx 0.39$, and this value is plotted as a dashed-dotted line in Fig. 3, showing a good agreement with the numerical simulations when P_2 is sufficiently large.

It should be noted that our choice of initial conditions in a circular state is not incidental. Indeed, since $m = n_0 - 1$

is conserved, the n_0 CRS is not "connected" from below to any other state (it is the "ground state" of the resonant chain). Therefore, the LZ transitions can only transfer the population up the resonant chain. However, if the initial conditions were chosen such that there existed a state below n_0, the sweeping driving frequency would have driven the population down to this state, and the excitation process would have stopped.

Lastly, one still needs to find the values of P_2 for which the LC framework is applicable. As mentioned above, the LZ transitions must be well separated in time so they can be treated as separate two-level transitions. To check when this condition is met, we follow the footsteps of [25] and [36] and compare the time between two successive LZ transitions and the time width of a single transition. The width of a single LZ transition can be estimated as $\Delta\tau_{LZ} = 1 + P_1 c_n^{+1}$ [36], while the time between two successive transitions can be found using Eq. (7), yielding $\Delta\tau_{between} \approx d^2\overline{E}_n/dn^2$. Therefore, the condition $\Delta\tau_{between} \gg \Delta\tau_{LZ}$ guarantees that the transitions are well separated. Explicitly, the condition reads

$$P_2\left(\frac{n_0}{n}\right)^4 \gg 1 + P_1 c_n^{+1}, \tag{10}$$

where again index l was omitted. For several initial LZ steps starting from some $n_0 \gg 1$, this condition can be relaxed by substituting n_0 for n and recalling that by construction $c_{n_0}^{+1} = 1$,

$$P_2 \gg 1 + P_1. \tag{11}$$

The solid line in the parameter space in Fig. 3 represents $P_2 = 1 + P_1$ and one can see that above this line the efficiency depends only on P_1, while $P_{1,th}^{LC}$ (dashed-dotted line in Fig. 3) bounds the region of an efficient LC process. Returning to Fig. 1, which exhibits LC-type evolution, one can see that its $P_{1,2}$ parameters are well inside the quantum region (the parameters are marked by the black circle in Fig. 3). If condition (11) is not satisfied, the transitions are not well separated and many states mix. This type of evolution is demonstrated in Fig. 2, where the parameters are well below the separation line (marked by the black diamond in Fig. 3). The nature of the evolution in this case is studied next.

B. Classical autoresonance

The previous subsection showed that quantum-mechanical analysis does not fully explain the results in Fig. 3. One can see in the figure two different threshold lines for efficient excitation. We show now that thedashed diagonal line corresponds to classical evolution. To understand this region in the parameter space, we turn to the classical analysis in Ref. [15]. We present the main results of [15] here for completeness, while reformulating this theory in terms of our dimensionless quantum-mechanical parameters $P_{1,2}$.

The classical problem of the driven atom is conveniently analyzed using the three pairs of action-angle variables of the unperturbed problem. The actions I_2 and I_1 are associated with the total angular momentum and its projection on the z axis, respectively, while the action I_3 characterizes the unperturbed Hamiltonian, which is proportional to I_3^{-2}. The semiclassical approximation then yields $I_3 \approx \hbar n$, $I_2 \approx \hbar l$, $I_1 \approx \hbar m$. The classical theory in [15] used the single-resonance
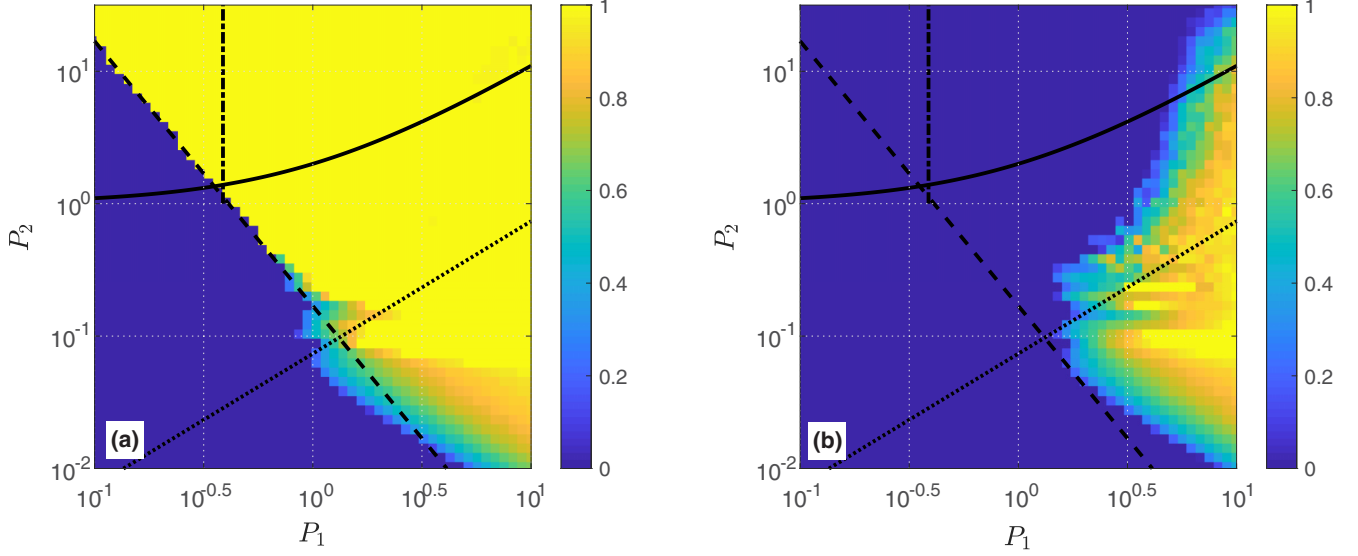
FIG. 4. Classical numerical simulations for the 1:1 resonance case, with parameters and initial conditions corresponding to Fig. 3. (a) Solution of the classical equations of motion for the fraction of initial conditions leading to $\bar{I}_3 > 50$ when starting from a circular orbit with $\bar{I}_{3,0} = 40$ and $\bar{I}_{1,0} = 40$. (b) Same as (a) but for the fraction of initial conditions leading to ionization. The initial (final) driving frequency matches the resonant frequency at $n = 30$ ($n = 60$). Dashed lines mark the classical threshold, (14). Solid lines mark the quantum-classical separation line, (11). Dotted lines mark the breakdown of the SRA, (15), for $\gamma = 1$, $n = n_f$. Dashed-dotted lines mark the value of $P_{1,th}^{LC}$ as calculated using Eq. (9).

approximation (a classical analog of the RWA). It resulted in a dimensionless Hamiltonian, which in terms of our parameters $P_{1,2}$ can be written as

$$H(\Theta_{1,2,3}, \bar{I}_{1,2,3}) = -\frac{P_2 n_0^4}{6\bar{I}_3^2} + \frac{\sqrt{2}P_1}{n_0^{3/2}}\bar{I}_3^2 \sin i \sin \Phi, \qquad (12)$$

where the actions are normalized by $\hbar$ ($\bar{I}_{1,2,3} = I_{1,2,3}/\hbar$), time is normalized by $1/\sqrt{\alpha}$, distances are normalized with respect to Bohr's radius a_0, i is the inclination angle ($\sin i = I_1/I_2$), and $\Phi = \Theta_3 + \Theta_2 - \phi_d$, with $\Theta_{2,3}$ being the angle variables corresponding to actions $I_{2,3}$. The physical meaning of the phase mismatch Φ is revealed when examining its temporal derivative

$$\frac{d\Phi}{d\tau} = \frac{d\Theta_3}{d\tau} + \frac{d\Theta_2}{d\tau} - \omega_d \approx \frac{d\Theta_3}{d\tau} - \omega_d + O(P_1). \qquad (13)$$

If $d\Phi/d\tau \approx 0$, the orbital frequency $d\Theta_3/d\tau$ approximately follows the driving frequency. This classical resonance condition is actually the same as the quantum one, (7), within the semiclassical approximation. It is shown in Ref. [15] that if the driving frequency starts sufficiently far from the resonance, Hamiltonian (12) yields a continued phase-locking $\Phi \approx 0$ after passage through resonance provided that (using our parametrization)

$$\sqrt{P_2}P_1 > 0.41. \qquad (14)$$

If this sharp threshold condition is satisfied, the resulting phase locking yields a continuous increase in the energy as the system self-adjusts to stay in resonance for an extended period of time. Note that the form of the left-hand side in the classical threshold condition, (14), could have been predicted even without the detailed analysis in [15], as it is the only combination of parameters $P_{1,2}$, which does not depend on $\hbar$

(which cancels out after we replace n_0 with the initial dimensionless I_3). We illustrate the sharp threshold phenomenon of the classical autoresonance in Fig. 4(a), showing the excitation efficiency as a function of parameters $P_{1,2}$ using the *exact* classical equations of motion (for details on these simulations see Appendix B). In order to check the independence of the capture of the system in autoresonance on the initial phase mismatch, we started the simulation on a circular orbit with spherical angles $\varphi = \theta = 0$, and averaged over the initial driving phase between 0 and 2π. All other parameters are the same as in Fig. 3. One can see that both the classical [Fig. 4(a)] and the quantum (Fig. 3) simulations correctly recreate the threshold condition (dashed line) even though the threshold region is much narrower in the classical results. Naturally, the classical simulations entirely ignore the quantum-classical separation (solid line) given by condition (11), further demonstrating the quantum nature of the evolution above the separation line and identifying the dashed line as the classical threshold. The broadening of the threshold region in Fig. 3 can be attributed to quantum fluctuations of the initial state, which were absent in the classical simulations.

The previous and current subsections describe *purely* LC or AR evolutions. However, as mentioned above, one must also consider an intermediate case where the initial evolution is of an LC nature (i.e., condition [11] is met), but in the final evolution stage condition (10) is violated and we expect a dynamical transition from LC to AR at later times. In fact, this situation was relevant to practically all of the region in Fig. 3 above the quantum-classical separation line. Nevertheless, as demonstrated in Fig. 1(b), the efficiency of the excitation remains high and smooth despite the transition from LC to AR. The reason for this smooth transition can be explained by observing that the LC process closely follows the resonance with the drive. In turn, this also means that at the transition to

the classical regime, the evolution is phase-locked to the drive and the classical phase mismatch Φ remains bounded. This guarantees smooth transition to the AR regime as the classical dynamics emerges during the chirped excitation process.

Finally, one can see in the lower-right part in Fig. 4(a) that the transition region to efficient excitation is not as narrow. We attribute this effect to the breaking of the SRA when parameter P_1 becomes large, as discussed in the next section.

C. The breaking of the single-resonance approximation and ionization

Our quantum-mechanical model does not include ionization channels, so we discuss the problem of ionization within the classical theory. Classically, the ionization in the driven-chirped problem can occur when the SRA loses its validity. This effect was studied in [15], where it is shown that the breakdown of the SRA happens when the frequency of oscillations of Φ in autoresonance become of the order of the driving frequency and other resonant terms become important. When this happens the dynamics is not dominated by the 1:1 resonance, and ionization may soon follow via chaotic dynamics. Based on [15] the condition for breakdown of the SRA is

$$\frac{P_1}{P_2} > \gamma \frac{n_0^{7/2}}{9\sqrt{2}\sqrt{1 - \left(\frac{m}{n}\right)^2 n^4}}, \tag{15}$$

where we have used the semiclassical approximation for the dimensionless actions and γ is a numerical factor smaller than 1. Condition (15) is again local and gets easier to satisfy for higher n. Therefore, for estimation, we substitute $n = n_f$ in (15), where n_f is the resonant value of n at the end of the excitation process. Figure 4(b) shows the classical ionization probability for the same parameters as in Fig. 4(a). The diagonal dotted line in the figure is given by Eq. (15) for $n = n_f$ and $\gamma = 1$. One can see that the ionization regime is centered around this line. Furthermore, our quantum-mechanical simulations in Fig. 3 are performed in the portion of the parameter space for which no ionization happens classically. In this part of the parameter space we do not expect ionization to occur.

In order to avoid destruction of AR at large n [see condition (15)], we limit the value of n_f, so that a sizable part of the parameter space avoids ionization. The value of n_{th} was taken halfway between n_0 and n_f to identify significant excitation.

V. 2:1 RESONANCE

Section IV revolved around analytic and numerical results for the 1:1 resonance, but the analysis is not limited to this choice. In this section, we show that the same considerations could be applied to the 2:1 resonance, leading to similar results. Consider a CRS initial condition defined by n_0 and m, such that m is not restricted and can take any value $|m| < n_0$. The choice of n_0 and n_{th} follows the same considerations as in Sec. IV. The driving frequency now sweeps through twice the Keplerian frequency, i.e., $2d\bar{E}_{n_0}/dn_0$, and the resonant transitions are $n, l, m \leftrightarrow n+2, l+1, m$. The analysis again starts with Eq. (6), but now for $q = 2$, so a two-level description similar to Eq. (8) follows immediately. The width of a single LZ transition and the time between two transitions are found

similarly to Sec. IV and the quantum-classical separation criterion is found to be

$$P_2\left(\frac{n_0}{n}\right)^4 \gg 1 + P_1 c_{n,l}^{+2}. \tag{16}$$

As with the 1:1 resonance, the initial stages of the evolution are the most important and condition (16) could be replaced by its version for $n = n_0$, yielding the same result as Eq. (11). Figure 5 shows numerical simulations for the efficiency of excitation by passage through the 2:1 resonance. Figure 5(a) shows quantum mechanical simulations for $n_0 = 90$, $m = 0$, while Fig. 5(b) shows classical simulations for the corresponding initial condition with $\bar{I}_3 = \bar{I}_2 = 90$ and $\bar{I}_1 = 0$. In the quantum simulations the efficiency is determined by the fraction of population exceeding $n_{\text{th}} = 100$, while for the classical simulations it is defined by the fraction of initial conditions out of a uniformly distributed initial phases that reach a final unperturbed energy corresponding to $\bar{I}_3 > 100$. Note that the range of $P_{1,2}$ in Fig. 5 is the same as that in Fig. 3.

The solid lines in Figs. 5(a) and 5(b) separate the quantum and classical regions of the evolution. One can again observe the two regimes in Fig. 5(a) separated by this line and the absence of this separation in the classical simulation in Fig. 5(b). The efficiency of the LC process above this separation line could be calculated similarly to Eq. (9) by successively multiplying the efficiencies of individual LZ transitions. Once again, because the coupling coefficients grow rapidly, the threshold value $P_{1,\text{th}}^{\text{LC}}$ for which the total efficiency is 0.5 depends only weakly on the number of transitions. It also depends rather weakly on the value of m. For example, the parameters $n_0 = 90$, $m = 0$ as in Fig. 5 yield $P_{1,\text{th}}^{\text{LC}} \approx 0.39$ (same as in Sec. IV), but when $m = 89$, $P_{1,\text{th}}^{\text{LC}} \approx 0.34$. The value of $P_{1,\text{th}}^{\text{LC}}$ is represented in Figs. 5(a) and 5(b) by dashed-dotted vertical lines. One can observe good agreement between the predictions of the quantum mechanical simulation and this line in Fig. 5(a).

It should be noted that like the 1:1 resonance in Sec. IV, the CRS studied here has the property that it is not "connected" from below to any other state along the resonant chain. The state below the initial condition in the chain would have had $n = n_0 - 2 = l$, which is not a physical state. Since this is true for every m, the 2:1 LC continuing excitation process could be applied to any m, unlike the 1:1 LC.

When condition (11) is violated, the classical dynamics emerges and one can use the results in [15] to find that the capture into classical AR is only possible when

$$\sqrt{P_2}P_1 > 0.41. \tag{17}$$

Remarkably, this result is identical to the one observed for the 1:1 resonance [Eq. (14)], demonstrating the uniqueness of the parametrization used in this work. The dashed lines in Fig. 5 show the threshold $\sqrt{P_2}P_1 = 0.41$ for efficient excitation. The classical simulations exhibit a sharp transition at this line, except for low P_2 as one gets closer to the breaking of the SRA (the corresponding breaking line, as in Fig. 4 is outside the range of the $P_{1,2}$ values in Fig. 5). In the quantum-mechanical simulations, the classical threshold is retrieved below the quantum-classical separation line, (11), but is broadened compared to the classical simulations due to quantum fluctuations.
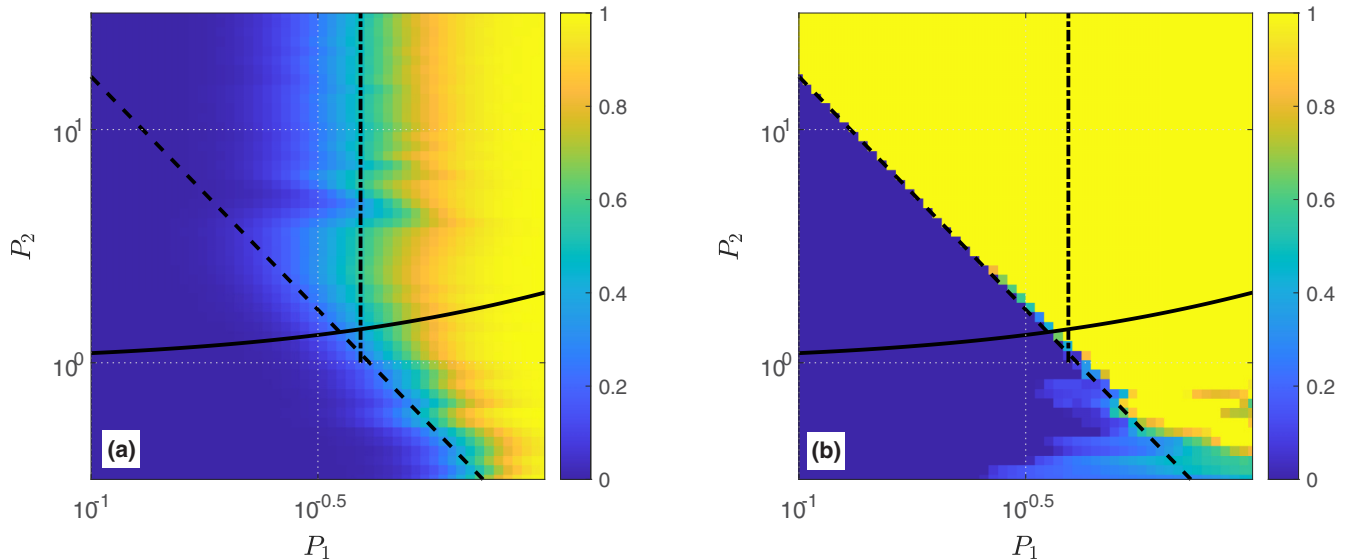
FIG. 5. Numerical simulations of the 2:1 resonance. (a) Solution of Eq. (6) for the fraction of population with $n > 100$ when starting from a circular state with $n_0 = 90$ and $m = 0$. (b) Solution of the classical equations of motion for the fraction of initial conditions leading to $\bar{I}_3 > 100$ when starting from a circular orbit with $\bar{I}_{3,0} = 90$ and $\bar{I}_{1,0} = 0$. In all simulations the initial (final) driving frequency matches the resonant frequency at $n = 80$ ($n = 110$). Dashed lines mark the classical threshold, (17). Solid lines show the quantum-classical separation line, (16), for $n = n_0$. Dashed-dotted lines mark the value of $P_{1,\text{th}}^{\text{LC}}$ as calculated using a modified version of Eq. (9) for the 2:1 resonance (see the text).

VI. SUMMARY

In conclusion, we have studied the problem of resonant excitation of a Rydberg atom starting in a CRS using chirped drive. Based on three characteristic time scales in the problem, we introduce two dimensionless parameters, $P_{1,2}$ [Eqs. (3) and (4)], and study the resonant nature of the problem in this parameter space within the rotating-wave approximation. We have shown how this approximation allows one to reduce the three-dimensional problem to one-dimensional resonant interactions characterized by the q:1 ratio ($q = 1, 2$) between the driving and the Keplerian frequencies. The 1:1 and 2:1 resonances are studied in detail, each showing two distinct persistent resonance regimes, i.e., the quantum-mechanical ladder-climbing and the classical autoresonance. The major criteria (borderlines) in the $P_{1,2}$ parameter space are discussed, including (a) the separation line between the two regimes and (b) the regions of efficient excitation in the two regimes. In both regimes very high efficiencies ($\sim 100\%$) are possible, but the LC process yields significantly narrower (in n) excited wave packets. Our analytic results are supported by classical and quantum-mechanical numerical simulations demonstrating the validity of our theoretical approach, as well as the quantum-classical correspondence and other effects such as quantum fluctuations. The ionization process in the chirped-driven excitation is discussed classically in the framework of breaking of the single-resonance approximation in the problem. It is shown that the ionization effect is negligible in the areas of interest in our quantum-mechanical simulations.

The results of this work extend previous studies of the chirped-driven Rydberg atom into the boundary between the quantum and the classical evolution. From a broader perspective, it is also the first use of the formalism for studying such quantum-classical transitions in a three-dimensional problem.

The processes described in this work enlarge the toolbox for the control and manipulation of Rydberg atoms and may lead to new applications. It will be interesting to study this problem for other initial conditions which are not CRS in the future. Generally speaking, such initial conditions should not exhibit sharp thresholds for capture into AR but, rather, a different capture process which could be conveniently studied in phase space [16,37]. Quantum mechanically, such initial conditions will not be the "ground state" of their resonant chain, so the climb up the energy ladder would require starting close to the resonance rather than sweeping through it. Another avenue for research could be studying time-varying chirp rates. The time between LZ transitions decreases by orders of magnitude as one climbs up the energy ladder, and thus, lowering chirps in time may allow us to prolong the LC process and reduce the possibility of ionization.

APPENDIX A: COUPLING COEFFICIENTS

In computing the coupling coefficients $\langle n, l, m | \hat{z} | n', l', m' \rangle$ we use the spherical coordinates r, θ, and φ and separate the integral for the coefficients into the radial and angular parts. The angular part is found by expressing z as a function of r and the spherical harmonic $Y_1^0(\theta, \varphi)$. The functions $\psi_{n',l',m'}$ and $\psi_{n,l,m}^*$ contribute two more spherical harmonics, and the product of the three could be integrated in terms of the Wigner $3j$ symbol, yielding the angular contribution, as well as the selection rules $m = m'$ and $l = l' \pm 1$. For the radial part we first normalize r by $m_e a_0 / 2\mu$, where a_0 is Bohr's radius and

μ the reduced mass (the normalization factor is absorbed into ε). The radial integral is then given by

$$\int_0^\infty r^3 R_{n,l}^*(r) R_{n',l'}(r) dr,$$

$$R_{n,l}(r) = \sqrt{\frac{(n-l-1)!}{2n^4[(n+l)!]}} e^{-\frac{r}{2n}} \left(\frac{r}{n}\right)^l L_{n-l-1}^{2l+1}\left(\frac{r}{n}\right),$$

where L_a^b is the generalized Laguerre polynomial. Note that L_a^b is a polynomial of order a, and therefore the product $r^3 R_{n,l}^*(r) R_{n',l'}(r)$ could be broken into the sum of $(n - l - 1) \times (n' - l' - 1)$ terms proportional to $r^k e^{-rp}$, where $k, p > 0$. The integral for each term yields $p^{-1-k}\Gamma(1+k)$, with Γ the Euler Gamma function. The final result reads

$$c_{n,l,m}^{n',l+1} = \frac{1}{2}\sqrt{\frac{(l-m+1)(l+m+1)}{(2l+3)(2l+5)}}$$

$$\times \sqrt{(n-l-1)!(n'-l-2)!(n+l)!(n'+l+1)!}$$

$$\times \sum_{i=0}^{n-l-1}\sum_{j=0}^{n'-l-2} f_i^{n,l} f_j^{n',l+1} D,$$

where

$$D = \left(\frac{2nn'}{n+n'}\right)^{2l+5+i+j} (2l+4+i+j)!,$$

$$f_i^{n,l} = (-1)^i [n^{i+l+2}(n-l-1-i)!(2l+1+i)!(i)!]^{-1}.$$

These $c_{n,l,m}^{n',l+1}$ were computed using a symbolic software, to avoid numerical accuracy issues. Note that the coupling of CRSs to other CRSs, or nearly circular states, contains only a small number of contributions and can by calculated explicitly. Namely, in the limit $n_0 \gg 1$ the value of C_0 is $\sqrt{2}n_0^{3/2}$ for the 1:1 resonance with $m = n_0 - 1$, and $\sqrt{1-(m/n_0)^2}n_0^{3/2}/\sqrt{2}$ for the 2:1 resonance.

APPENDIX B: NUMERICAL SIMULATIONS

The quantum-mechanical simulations in Figs. 1 and 2 use Eq. (5). The maximal value of n and $n - l$ was chosen such that only a negligible portion of the population reaches the states along those numerical boundaries in the Hilbert space. The simulations in Figs. 3 and 5(a), however, are based on the RWA [Eq. (6)], i.e., include only the states which are connected to the initial condition through the resonant interaction. This validity of this assumption improves as P_2 increases and breaks down completely in the portion of the parameter space where ionization occurs. For this reason the quantum mechanical simulations are limited to the region of the parameter space where no ionization is observed (classically). For the 1:1 resonance we have also tested the effect of the RWA by solving the same equation set with more states outside the resonant chain (i.e., states with higher values of $n - l$) and found no significant changes in the results presented in Fig. 3.

Our classical simulations are based on solving the classical Hamilton equations for the Hamiltonian,

$$H = \frac{P_2 n_0^4}{6q^2}\left[p_r^2 + \frac{p_\theta^2}{r^2} + \frac{p_\phi^2}{r^2\sin^2\theta} - \frac{2}{r}\right] + \frac{2P_1}{C_0}\cos\phi_d r \cos\theta,$$

where r, θ, and ϕ are spherical coordinates and p_r, p_θ, and p_ϕ their conjugate momenta. Naturally, the quantum-mechanical initial condition does not translate directly to a classical initial condition. We used initial conditions corresponding to a classical circular Keplerian case but averaged over the initial driving phase ϕ_d between 0 and 2π in Fig. 4 and over θ between 0 and π in Fig. 5(b) for testing the validity of the single-resonance approximation. One can observe that in both figures all initial conditions yield the same results except for the bottom-right corner of the parameter space, where the SRA is not valid.

[1] J. Lim, H. G. Lee, and J. Ahn, J. Korean Phys. Soc. **63**, 867 (2013).

[2] S. Gleyzes, S. Kuhr, C. Guerlin, J. Bernu, S. Deléglise, U. B. Hoff, M. Brune, J. M. Raimond, and S. Haroche, Nature **446**, 297 (2007).

[3] D. H. Meyer, K. C. Cox, F. K. Fatemi, and P. D. Kunz, Appl. Phys. Lett. **112**, 211108 (2018).

[4] J. A. Sedlacek, A. Schwettmann, H. Kübler, R. Löw, T. Pfau, and J. P. Shaffer, Nat. Phys. **8**, 819 (2012).

[5] D. A. Anderson, S. A. Miller, G. Raithel, J. A. Gordon, M. L. Butler, and C. L. Holloway, Phys. Rev. Appl. **5**, 034003 (2016).

[6] M. Saffman, T. G. Walker, and K. Molmer, Rev. Mod. Phys. **82**, 2313 (2010).

[7] R. G. Hulet and D. Kleppner, Phys. Rev. Lett. **51**, 1430 (1983).

[8] D. Delande and J. C. Gay, Europhys. Lett. **5**, 303 (1988).

[9] C. H. Cheng, C. Y. Lee, and T. F. Gallagher, Phys. Rev. Lett. **73**, 3078 (1994).

[10] A. Signoles, E. K. Dietsche, A. Facon, D. Grosso, S. Haroche, J. M. Raimond, M. Brune, and S. Gleyzes, Phys. Rev. Lett. **118**, 253603 (2017).

[11] C. Guerlin, J. Bernu, S. Deleglise, C. Sayrin, S. Gleyzes, S. Kuhr, M. Brune, J. M. Raimond, and S. Haroche, Nature **448**, 889 (2007).

[12] C. Sayrin, I. Dotsenko, X. Zhou, B. Peaudecerf, T. Rybarczyk, S. Gleyzes, P. Rouchon, M. Mirrahimi, H. Amini, M. Brune, J. M. Raimond, and S. Haroche, Nature **477**, 73 (2011).

[13] T. L. Nguyen, J. M. Raimond, C. Sayrin, R. Cortiñas, T. Cantat-Moltrecht, F. Assemat, I. Dotsenko, S. Gleyzes, S. Haroche, G. Roux, Th. Jolicoeur, and M. Brune, Phys. Rev. X **8**, 011032 (2018).

[14] J. Lambert, M. W. Noel, and T. F. Gallagher, Phys. Rev. A **66**, 053413 (2002).

[15] E. Grosfeld and L. Friedland, Phys. Rev. E **65**, 046230 (2002).

[16] A. Neishtadt and A. Vasiliev, Phys. Rev. E **71**, 056623 (2005).

[17] R. M. W. van Bijnen, S. Smit, K. A. H. van Leeuwen, E. J. D. Vredenbregt, and S. J. J. M. F. Kokkelmans, J. Phys. B **44**, 184008 (2011).

[18] J. Preclíková, M. Kozák, D. Fregenal, Ø. Frette, B. Hamre, B. T. Hjertaker, J. P. Hansen, and L. Kocbach, Phys. Rev. A **86**, 063418 (2012).

[19] J. Fajans and L. Friedland, Am. J. Phys. **69**, 1096 (2001).

[20] L. D. Landau, Phys. Z. Sowjetunion **2**, 46 (1932).

[21] C. Zener, Proc. R. Soc. London A **137**, 696 (1932).

[22] S. Chelkowski and G. N. Gibson, Phys. Rev. A **52**, R3417 (1995).

[23] D. J. Maas, D. I. Duncan, R. B. Vrijen, W. J. van der Zande, and L. D. Noordam, Chem. Phys. Lett. **290**, 75 (1998).

[24] G. Marcus, A. Zigler, and L. Friedland, Europhys. Lett. **74**, 43 (2006).

[25] G. Marcus, L. Friedland, and A. Zigler, Phys. Rev. A **69**, 013407 (2004).

[26] T. Armon and L. Friedland, Phys. Rev. A. **96**, 033411 (2017).

[27] Y. Shalibo, Y. Rofe, I. Barth, L. Friedland, R. Bialczack, J. M. Martinis, and N. Katz, Phys. Rev. Lett. **108**, 037701 (2012).

[28] I. Barth, I. Y. Dodin, and N. J. Fisch, Phys. Rev. Lett. **115**, 075001 (2015).

[29] K. Hara, I. Barth, E. Kaminski, I. Y. Dodin, and N. J. Fisch, Phys. Rev. E **95**, 053212 (2017).

[30] T. Armon and L. Friedland, Phys. Rev. A **100**, 022106 (2019).

[31] G. Manfredi, O. Morandi, L. Friedland, T. Jenke, and H. Abele, Phys. Rev. D **95**, 025016 (2017).

[32] B. Meerson and L. Friedland, Phys. Rev. A **41**, 5233 (1990).

[33] W. H. Li, I. Mourachko, M. W. Noel, and T. F. Gallagher, Phys. Rev. A **67**, 052502 (2003).

[34] J. Zhao, H. Zhang, Z. Feng, X. Zhu, L. Zhang, C. Li, and S. Jia, J. Phys. Soc. Japan **80**, 034303 (2011).

[35] To calculate the exact values of the minimal n value, one has to use the full form of τ_n^q, which fulfills exactly $\Gamma_{n,l} = \Gamma_{n+q,l+1}$, and not the approximated form derived from Eq. (7).

[36] I. Barth, L. Friedland, O. Gat, and A. G. Shagalov, Phys. Rev. A **84**, 013837 (2011).

[37] T. Armon and L. Friedland, Phys. Rev. A **93**, 043406 (2016).